

## Article

# Annually Spatial Pattern Dynamics of Forest Types under a Rapid Expansion of Impervious Surfaces: A Case Study of Hangzhou City

Yuxin Zhu <sup>1</sup>, Jingchuan Zhou <sup>1</sup>, Mingyue Liu <sup>2</sup> , Weidong Man <sup>2</sup>  and Lin Chen <sup>1,\*</sup> 

<sup>1</sup> Zhejiang Provincial Key Laboratory of Urban Wetlands and Regional Change, Institute of Remote Sensing and Earth Sciences, Hangzhou Normal University, Hangzhou 311121, China; zhuyuxin@stu.hznu.edu.cn (Y.Z.); zhoujingchuan@stu.hznu.edu.cn (J.Z.)

<sup>2</sup> Hebei Key Laboratory of Mining Development and Security Technology, Hebei Industrial Technology Institute of Mine Ecological Remediation, College of Mining Engineering, North China University of Science and Technology, Tangshan 063210, China; liumy917@ncst.edu.cn (M.L.); manwd@ncst.edu.cn (W.M.)

\* Correspondence: chenlin@hznu.edu.cn; Tel.: +86-0571-28869966

**Abstract:** Dramatic forest dynamics strongly influence pressure mitigation from the increasing population and climate changes of an urban landscape. Effectively monitoring landscapes in a spatiotemporally consistent manner, satellite remote sensing has emerged as the first analytical tool to help us understand the changes in urban forests. At present, most studies focus on classification algorithms, spatial analysis methods, and ecosystem models, and the literature lacks spatiotemporally explicit research on the responses of different types of forests to urbanization. Thus, in this study, Hangzhou was selected as a typical metropolitan area to determine the annual spatial patterns of urban forests at a forest-type level. To illustrate the spatial pattern dynamics of different forest types resulting from rapid urbanization, this study characterized the Landsat-based spatial patterns of different forest types, as well as their annual changes from 2000 to 2022 using object-based backdating classification, land-use transfer matrix, area-weighted centroids, and landscape pattern indexes. The spatiotemporal effects of impervious surface expansion on forest pattern changes at a type scale were discussed. The results demonstrated that forests, mainly located in the southwest, decreased from 11,660.69 to 11,516.15 km<sup>2</sup>. Moreover, evergreen broadleaved forests occupied the largest area and had the most decreased ratio among the three forest types over 23 years, followed by evergreen needle-leaved and deciduous broadleaved forests. In total, 103.37 km<sup>2</sup> of forest areas transformed to impervious surfaces, with the highest annual transformation of area occurring among evergreen broadleaved forests widely across Hangzhou City and the lowest occurring among deciduous broadleaved forests. Forests lost adjacency due to the development of Hangzhou City, while this southwestward shrinkage slowed down over 23 years, resulting in the highest increase in the degree of evergreen broadleaved forest fragmentation. Therefore, measures of city planning according to the deep effects of adjustments of administrative divisions to forest suitability should be implemented, such as green ecological corridor construction. This research provides a Landsat-based methodology at a spatiotemporally explicit-scale perspective for better understanding forest changes under high-speed urbanization.

**Keywords:** annual forest type maps; forest spatiotemporal patterns; forestry effects of urbanization; Landsat series; Google Earth Engine; Hangzhou City



**Citation:** Zhu, Y.; Zhou, J.; Liu, M.; Man, W.; Chen, L. Annually Spatial Pattern Dynamics of Forest Types under a Rapid Expansion of Impervious Surfaces: A Case Study of Hangzhou City. *Forests* **2024**, *15*, 44. <https://doi.org/10.3390/f15010044>

Academic Editor: Pedro Álvarez-Álvarez

Received: 10 December 2023

Revised: 19 December 2023

Accepted: 22 December 2023

Published: 24 December 2023



**Copyright:** © 2023 by the authors. Licensee MDPI, Basel, Switzerland. This article is an open access article distributed under the terms and conditions of the Creative Commons Attribution (CC BY) license (<https://creativecommons.org/licenses/by/4.0/>).

## 1. Introduction

Booming urbanization has notably harmed the natural ecosystem through the replacement of natural surfaces with artificial impervious surfaces, altering the surface thermal environment and hydrological cycle [1,2]. These globally expanding impervious surfaces support growing urban populations, creating opportunities for forests to deliver crucial

ecosystem services and mitigate environmental impacts, such as urban heat islands and waterlogging [3–5]. These services depend on the forest type, which is shaped by responses to environmental processes and a diverse supply of wildlife and human habitats and resources [6,7]. Therefore, subjects related to the spatiotemporal patterns of urban forest types have attracted widespread attention among international scholars and organizations [8,9].

The traditional field-observed regional mapping of urban forest types is precise but costly. Satellite remote sensing techniques, such as optical sensors of Moderate Resolution Imaging Spectroradiometer (MODIS), Landsat series, and Sentinel-2, provide spatially explicit forest observations in a comparable and repeatable manner [10,11]. On account of the comparatively finer spatial resolution with a long-time sequence, the Landsat series has become a popular data source for characterizing forest dynamics [12–14]. Furthermore, Google Earth Engine (GEE) is a powerful geo-big data computing platform that combines spatiotemporally spectral features for large-scale forest-type classification and produces a series of multi-scale maps [15–17]. Zhang et al. [18] developed a Landsat-based global 30 m land-use map with a detailed classification system of forest types using the metric composite method on GEE and a multi-temporal random forest model, of which the overall accuracy is 82.5%. IokiAn et al. [19] investigated the use of the Landsat series to identify the characteristics of disturbance events during the recovery of tree community composition. Then, the spatiotemporal patterns of urban forests were commonly quantified via the spatial analysis of temporal dynamics within the forest area, distribution, transformations, and landscape pattern indexes [20–22]. Shen et al. [23] adopted object-oriented Landsat-based mapping of an urban forest cover and analyzed dynamics employing a transfer matrix. Kowe et al. [24] acquired detailed information on urban vegetation patches and their landscape metrics with the help of Landsat images to further examine the impact on urban thermal cooling. Yang et al. [25] assessed the influence of urbanization on vegetation in China based on the type of conversions and spatial centroids. Overall, previous studies have closely studied classification algorithms and spatiotemporal conversions from forests to impervious surfaces, as well as the driving forces [26–28]. Despite these great strides in remote-sensing-based spatial analysis, the link between forest changes and urban expansion was historically quantified at a whole-forest scale in most published papers. Namely, the spatiotemporally explicit response of forest types to rapid urbanization is not well documented.

Hangzhou earned its reputation as an International Garden City and National Forest City due to its urban greening efforts with a high rate of vegetation covers [29,30]; nevertheless, urban development soared from 23% in 1978 to 84% in 2022 [31]. With the booming urbanization process, forest dynamics have caught an additional focus in government planning efforts toward the construction of Hangzhou's forest city and poly-centric urban structures [30,32]. Prior studies were limited in observing forest changes under urbanization before 2020, with at least a five-year interval, and they mostly applied land-use classification at the first level. Nevertheless, precise up-to-date forest dynamics at a type scale following impervious surface expansion in Hangzhou City require further exploration. Most notably, spatiotemporally explicit responses of various forest types to urbanization have been insufficiently researched but remain crucial in supporting government planning to balance urbanization and forest management in Hangzhou City. As such, the specific objectives of this study were to: (1) map the annual spatial distributions of various forest types; (2) quantify the spatiotemporal transformation of different forest types to impervious surfaces; and (3) analyze the relationship of spatiotemporal patterns between the forest type and impervious surface.

## 2. Materials and Methods

### 2.1. The Study Area

As the capital of the Zhejiang Province in China and the second largest metropolis in the Yangtze River Delta, Hangzhou City is located between 118°20'23"–120°42'50" E and 30°33'54"–29°11'19" N, in the lower reaches of the Qiantang River (Figure 1). The

area includes 10 districts, two counties, and one county-level city, covering an area of 16,846.92 km<sup>2</sup> [33]. This region encompasses a vegetation zone named subtropical evergreen broad leaved forests and has a humid subtropical monsoon climate with four distinct seasons, including hot and humid summers and cold and dry winters [34,35]. It has an annual average temperature of 17 °C and annual precipitation of 1450 mm [36]. Over the past two decades, characterized by its economic soar, Hangzhou City has undergone high-speed urbanization, with the urban population rising from 3.73 million in 2000 to 10.39 million in 2022 [31,32]. At the same time, this region has experienced intense land-use changes with the expansion of impervious surfaces, with consequential environmental impacts, such as urban inland inundation, heat island formation, and decreasing vegetation carbon storage [37–39].

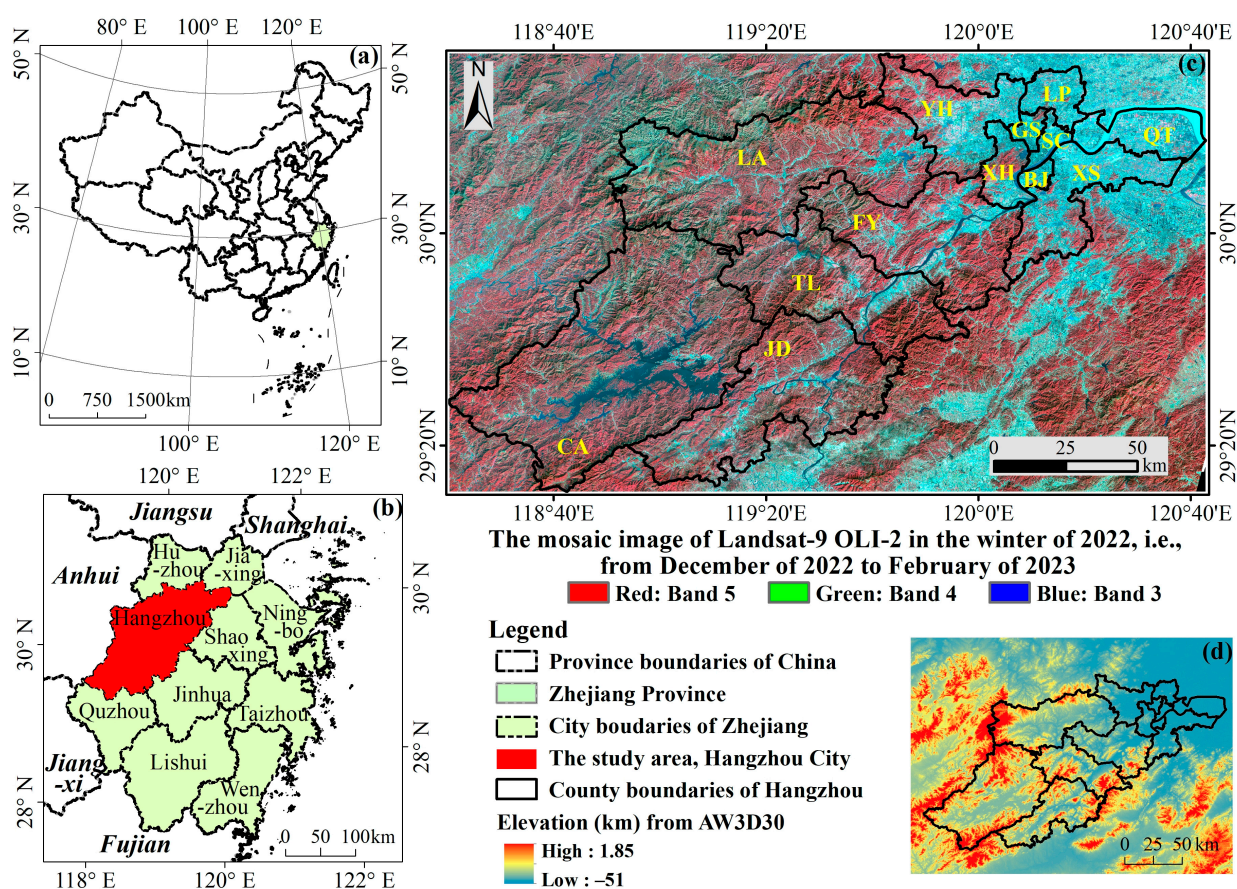


**Figure 1.** The location (a,b) and mosaic image (c) of the Landsat-9 OLI-2 in the winter of 2022 and elevation (d) from the Advanced Land Observing Satellite World 3D-30 m (AW3D30) of the study area. Here, SC, GS, XH, BJ, LP, QT, XS, YH, LA, FY, TL, JD, and CA represent districts named Shangcheng, Gongshu, Xihu, Binjiang, Liping, Qiantang, Xiaoshan, Yuhang, Li'an, and Fuyang and counties named Tionglu, Jiande and Chun'an, respectively.

## 2.2. Data and Preprocessing

A total of 1666 satellite images from 2000 to 2022 were used in this study, including ones derived from the Landsat Thematic Mapper (TM), Enhanced Thematic Mapper Plus (ETM+), Operational Land Imager (OLI), and OLI-2 imagery (Table S1). For mapping forest types and impervious surfaces, Landsat surface reflectance tier 1 images were chosen and processed using the simpleComposite function to obtain and download mosaic images based on the GEE cloud-computing platform (Figure 2) [40]. To classify the forest type, mosaic images taken during the summer and winter were separately produced, with the exception of images from 2012. Due to a lack of satisfactory images in different seasons

of 2012, a yearly mosaic image was used for classification. The summer mosaic image was computed from June 1st to August 31st, and the winter was defined as the period from December 1st to the end of February of the following year. The classification was based on the best-quality image with the lowest cloud cover in the study area among the multi-sensor and multi-season mosaic images, and the remaining mosaic images were used as auxiliary data. The mosaic image from the Landsat-9 OLI-2 in summer of 2022 is shown in Figure 1.

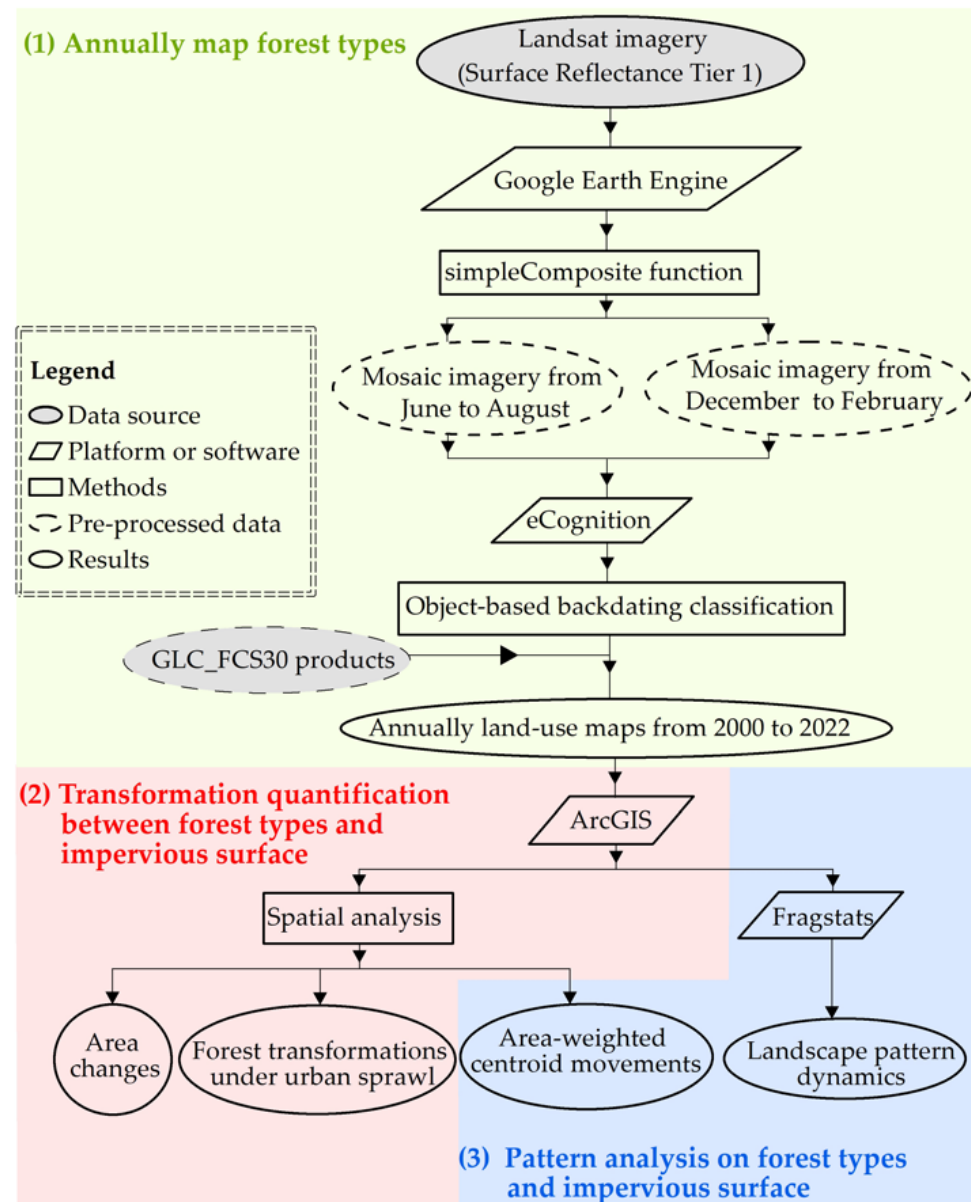


**Figure 2.** The outline of the quantification of the spatiotemporally explicit response of forest types to rapid urbanization. The version number of the software are follows as eCognition Developer 9.0, ArcGIS 10.2 and Fragstats 4.2.

The GLC\_FCS30 products of 2020 with the mapsheet names of E115\_30, E115\_35, E120\_30, and E120\_35 were downloaded from the Big Earth Data Science Engineering Program (<https://data.casearth.cn/>, accessed on 4 January 2022) as the baselines for the classification. These 30 m resolution global land-cover data products achieved a total accuracy of 82.5% and a Kappa coefficient of 0.78 [18].

### 2.3. Methods

The workflow of this study, shown in Figure 2, was composed of three parts: (1) annual mapping of the forest types and impervious surfaces via the object-based backdating classification; (2) quantifying spatiotemporal dynamics of different forest types under the expansion of impervious surfaces employing the land-use transfer matrix and spatial centroid; and (3) analyzing the relationships of the spatiotemporal patterns of diverse forest types and impervious surfaces by calculating the landscape pattern indexes.

#### 2.3.1. Object-Based Backdating Classification

An object-based backdating approach, according to existing mapping efforts, with a consistent classification scheme, improved the accuracy by decreasing pseudo changes and heterogeneity [32,41]. According to the classification system of GLC\_FCS30 products, land-use types in Hangzhou City were reclassified as evergreen broadleaved forests, deciduous broadleaved forests, evergreen needle-leaved forests, impervious surfaces, and other lands. To effectively implement annual mapping with a consistent classification scheme, the object-based backdating method was used to annually map forest types and impervious surfaces between 2020 and 2022, with the recognition of existing efforts. The classification accuracy was acceptable at overall values over 85%, which was assessed according to randomly selected samples from Google Earth images. Classification involved the following steps:

1. Object-based image analysis: The GLC\_FCS30 map of 2020, as Phase I data, and Landsat-9 OLI-2 mosaic image of 2022, as Phase II data, were segmented together by the eCognition Developer 9.0 software with 50, 0.1, and 0.5 as values of the scale, shape, and compactness, respectively.
2. Stratified image classification: The classes of objects from Phase II data were assigned according to those from Phase I data.
3. Visual interpretation and manual modification: The changed objects from Phase II data were modified manually to obtain the final map of 2022 at a 30 m spatial resolution.
4. Backdating: The final map of 2022 was used as the Phase I data, and the Landsat-8 OLI mosaic image of 2021 was used as the Phase II data. Steps from 1 to 3 were conducted to acquire the map for 2021. Based on the map of the Year  $N$  (as Phase I data) and the Landsat mosaic image of  $N-1$  (as Phase II data), steps from 1 to 3 were conducted to acquire the map for  $N-1$ .

#### 2.3.2. Land-Use Transfer Matrix

The land-use transfer matrix was widely computed to quantify the area conversions among diverse land-use types [42]. To characterize the contributions of impervious surfaces to the dynamics of different forest types in Hangzhou City, the following land-use transfer matrix was calculated using the tabulate area tool in the ArcGIS 10.2 software:

$$S_{ij} = \begin{pmatrix} S_{11} & \cdots & S_{1n} \\ \vdots & \ddots & \vdots \\ S_{n1} & \cdots & S_{nn} \end{pmatrix} \quad (1)$$

where  $S_{ij}$  is the area of land-use type  $i$  transferred to land-use type  $j$ , and  $n$  is the number of land-use types. In this study,  $n$  was 5.  $i$  and  $j$  (1, 2, ..., 5) represented land-use types before and after a certain transfer process, respectively. The contributions of other land-use types to the dynamics of different forest types represent the values from one of the columns in this matrix.

### 2.3.3. Area-Weighted Centroids

The area-weighted centroid is a set of the coordinates determined according to the area-weighted geometric center of polygons [43]. These spatial centroids of different forest types and impervious surfaces were mapped to delineate the direction of changes as follows:

$$\begin{cases} X_t = \sum_{i=1}^N (C_{ti} \cdot X_i) / \sum_{i=1}^N C_{ti} \\ Y_t = \sum_{i=1}^N (C_{ti} \cdot Y_i) / \sum_{i=1}^N C_{ti} \end{cases} \quad (2)$$

where  $X_t$  and  $Y_t$  are the longitude and latitude of a centroid of different forest types or impervious surfaces in year  $t$ , respectively;  $C_{ti}$  is the area of patch  $i$  in year  $t$  when calculating the centroid of different forest types or impervious surfaces;  $X_i$  and  $Y_i$  are the longitude and latitude of patch  $i$  used for different forest types or impervious surfaces, respectively; and  $N$  is the total patch number of different forest types or impervious surfaces. If different forest types or impervious surfaces grow or reduce equally in every direction, the area-weighted centroid remains invariant; otherwise, its centroid moves toward the direction in which the forest types or impervious surfaces expand or decrease more.

### 2.3.4. Landscape Pattern Indexes

Most rapidly growing populations dwell in cities and exert more pressure on urban forests, causing vegetation fragmentation and loss of landscape connectivity [24,44]. To quantify landscape configuration, the indexes referring to the relevant literature were calculated by employing the Fragstats 4.2 software as shown in Table 1 [45–47]. The dominance, complex, aggregation, fragmentation, and homogeneity were described by these typical indexes at class and landscape levels. Four land-use types were separately analyzed at a class level, including evergreen broadleaved forests, deciduous broadleaved forests, evergreen needle-leaved forests, and impervious surfaces. Landscape-level indexes were calculated for the entire study area and forests, respectively.

**Table 1.** Descriptions of adopted landscape pattern indexes.

Level	Type	Indexes	Formula	Description
	Area and edge	PLAND	$\frac{\sum_{j=1}^n a_{ij}}{A} \times 100$ ; $a_{ij}$ is the area of patch $ij$ ; $n$ is the total patch number of class $i$ ; $A$ is the total landscape area.	The class that obtains a greater PLAND occupies more area of the landscape.
		LPI	$\frac{\max_{j=1}^n (a_{ij})}{A} \times 100$ ; parameters present the same as the above.	The greater LPI class obtains the largest patch of the landscape.
Class	Shape	FRAC_AM	$FRAC = \frac{2 \ln(0.25 p_{ij})}{\ln a_{ij}}$ ; $p_{ij}$ is the perimeter of patch $ij$ ; the others present the same as the above; FRAC_AM is an area-weighted mean of FRAC.	The greater FRAC_AM class obtains the most complex shape across the landscape.
		LSI	$\frac{0.25 \sum_{k=1}^m e_{ik}^*}{\sqrt{A}}$ ; $e_{ik}^*$ is the total length of the edge in the landscape between classes $i$ and $k$ ; $m$ is the class number; the others present the same as the above.	The smaller LSI class shows the stronger aggregation across the landscape.
	Aggregation	PD	$\frac{n_i}{A} \times 10,000 \times 100$ ; $n_i$ is the patch number of class $i$ ; the others present the same as the above.	The greater PD class shows the worse fragmentation.
		SPLIT	$\frac{A^2}{\sum_{j=1}^n a_{ij}^2}$ ; parameters present the same as the above.	The greater SPLIT class shows the worse fragmentation.

Table 1. Cont.

Level	Type	Indexes	Formula	Description
Area and edge		ED	$\frac{E}{A} \times 10,000$ ; $E$ is the total length of the edge in the landscape; the others present the same as the above.	It describes the edge effect and landscape fragmentation.
		LPI	$\frac{\max(a_{ij})}{A} \times 100$ ; parameters present the same as the above.	The greater LPI indicates that the dominance is more outstanding.
Shape		FRAC_AM	FRAC_AM is the area-weighted mean of FRAC of all classes.	It describes the shape complexity across the landscape.
Landscape		LSI	$\frac{0.25E^*}{\sqrt{A}}$ ; $E^*$ is the total length of the edge in the landscape; the others present the same as the above.	It measures the overall geometric complexity of the landscape.
		PD	$\frac{N}{A} \times 10,000 \times 100$ ; $N$ is the total patch number in the landscape; the others present the same as the above.	It describes the landscape fragmentation.
	Aggregation	SPLIT	$\frac{A^2}{\sum_{i=1}^m \sum_{j=1}^n a_{ij}^2}$ ; parameters present the same as the above.	It describes the landscape fragmentation.
		CONTAG	$\left[ 1 + \frac{\sum_{i=1}^m \sum_{k=1}^m \left[ P_i \left( \frac{s_{ik}}{\sum_{k=1}^m s_{ik}} \right) \right] \cdot \left[ \ln \left( P_i \left( \frac{s_{ik}}{\sum_{k=1}^m s_{ik}} \right) \right) \right]}{2 \ln(m)} \right] \times 100$ ; $P_i$ is the proportion of the landscape occupied by class $i$ ; $s_{ik}$ is the number of adjacencies between the pixels of classes $i$ and $k$ based on the double-count method; the others present the same as the above.	It describes the landscape aggregation.
Diversity		SHDI	$\sum_{i=1}^m (P_i \cdot \ln P_i)$ ; parameters present the same as the above.	It describes the diversity at the landscape level.
		SHEI	$\frac{-\sum_{i=1}^m (P_i \cdot \ln P_i)}{\ln m}$ ; parameters present the same as the above.	It is the complement of dominance.

### 3. Results

#### 3.1. Spatiotemporal Distribution of Forests with the Expansion of Impervious Surfaces

Between 2000 and 2022, forest area decreased from 11,660.69 to 11,516.15 km<sup>2</sup>, with impervious surfaces exploding across Hangzhou City, and this mostly occurred in the southwest, i.e., Chun’an, Li’an and Jiande (Figures 3 and 4). Forests showed a slower reduction, with some fluctuations over 23 years under the decelerated urbanization of Hangzhou City, with the expansion rate being 27.95 km<sup>2</sup>/year in the first 10 years and 13.32 km<sup>2</sup>/year in the most recent 12 years (Figure 4a). The fastest changes appeared within the first 10 years, especially between 2006 and 2007 for forests and between 2007 and 2008 for impervious surfaces. Evergreen broadleaved forests had been occupying the largest area among the three forest types for 23 years, followed by evergreen needle-leaved and deciduous broadleaved forests (Figure 4a). At the same time, during the 2000–2022 period, the greatest decline of 1.41% was shown in evergreen broadleaved forests, and evergreen needle-leaved forests were reduced by 1.18%. The decrease ratio of deciduous broadleaved forests was the lowest, at 0.14%.

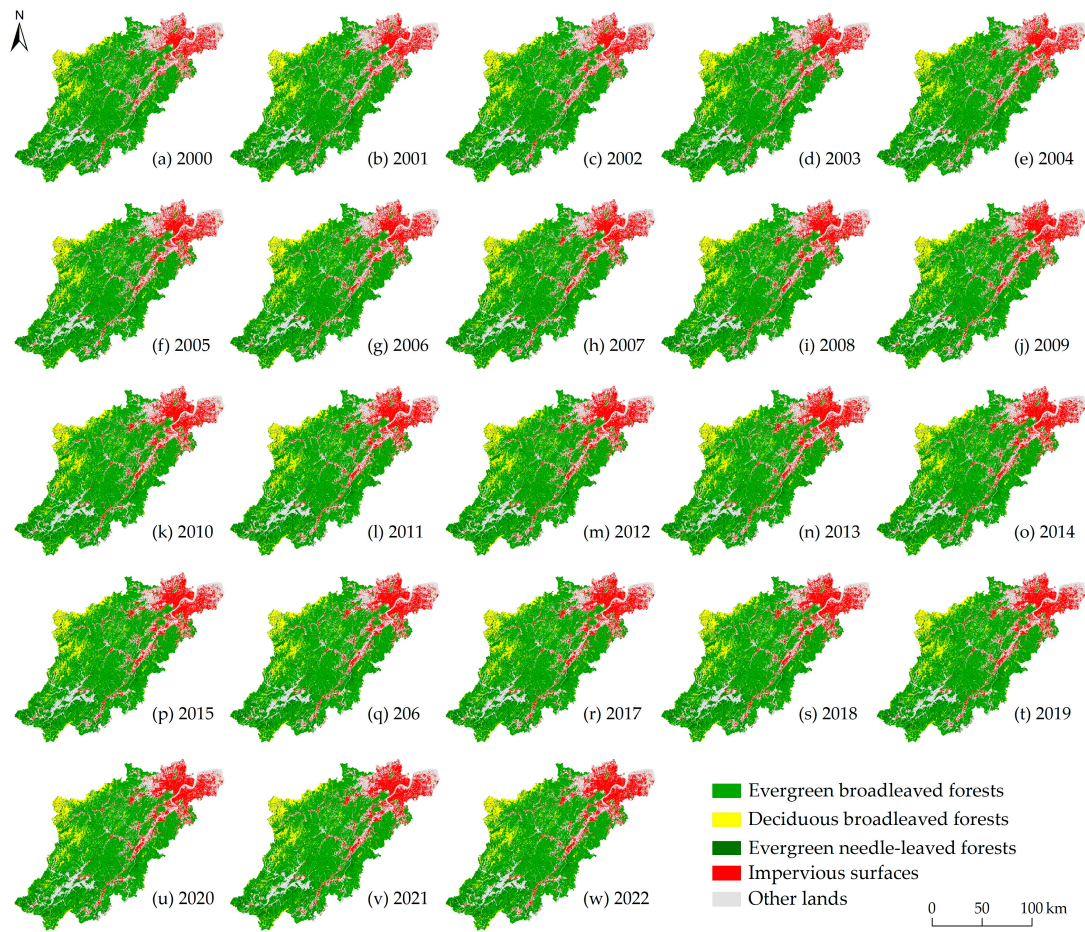


Figure 3. Annual land-use maps of Hangzhou City between 2000 and 2022.

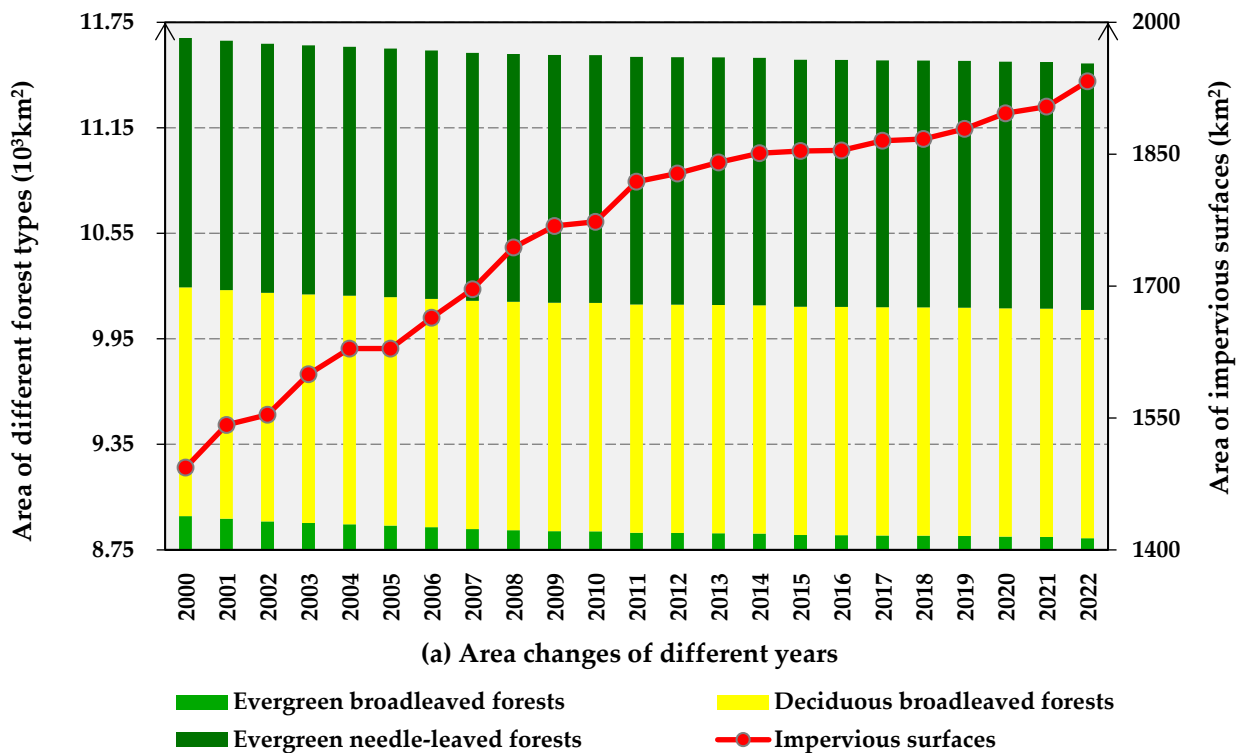
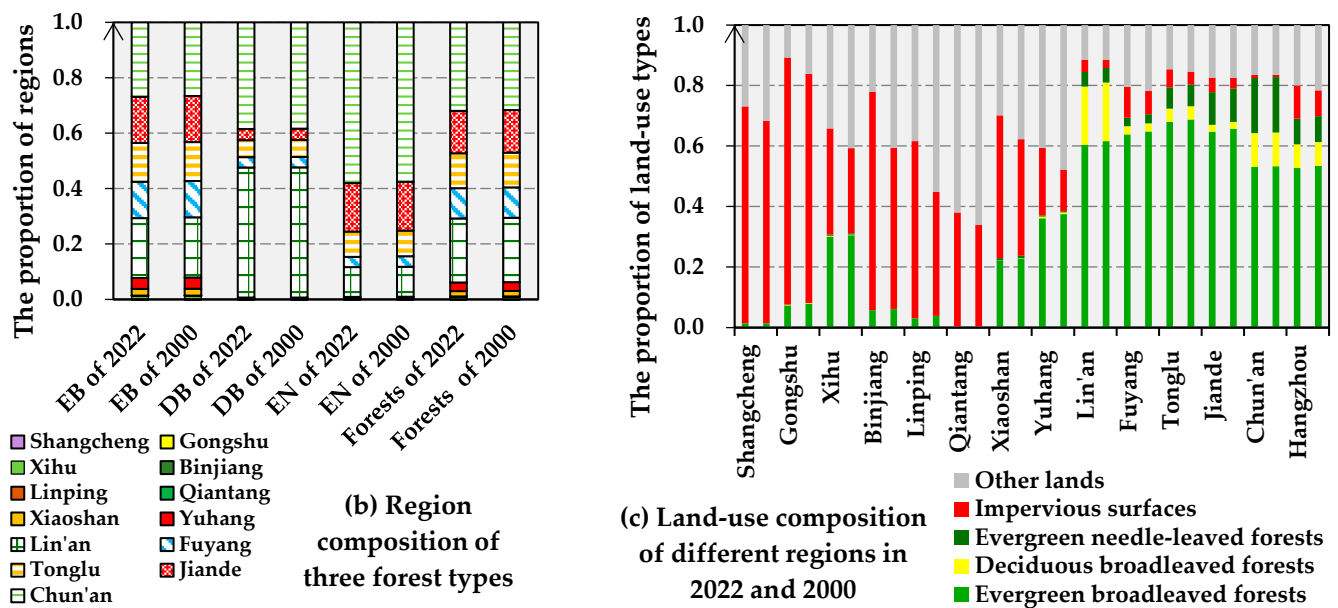


Figure 4. Cont.



**Figure 4.** Statistics of forest changes during the urban expansion of Hangzhou City between 2000 and 2022, including the annual area changes in forest types and impervious surfaces (a), and the composition dynamics of regions (b) and land-use types (c). The abbreviations EB, DB, and EN represent evergreen broadleaved, deciduous broadleaved, and evergreen needle-leaved forests, respectively.

The composition of forests in different regions slightly changed (Figure 4b,c). Evergreen broadleaved forests were chiefly distributed in Chun'an, Li'an, and Jiande. Li'an, Chun'an, and Tonglu encompassed most of the deciduous broadleaved forests. Evergreen needle-leaved forests mostly grew in Chun'an, Jiande, and Lin'an. Regarding the percentage of forests during period of 2000–2022, evergreen broadleaf area lowered from 76.68% to 76.55%, and deciduous broadleaf forest area increased from 11.15% to 11.27%, while evergreen needle-leaf remained at 12.17% with a slight increase. The forest dynamics mostly appeared in newly developed urban areas, such as Lin'an, Fuyang, Tonglu, and Jiande. Older regions, such as Shangcheng, Gongshu, Xihu, Binjiang, Linping, and Qiantang, showed that land-use changes mainly occurred for impervious surfaces and other lands. Outstanding changes in forests and impervious surfaces in Xiaoshan and Yuhang were observed. The land-use of Chun'an was observed to be quite stable for 23 years.

### 3.2. Spatiotemporal Transformation from Different Types of Forests to Impervious Surfaces

The annual occupation of forests by impervious surfaces was acquired using a land-use transfer matrix, as illustrated in Figure 5. Between 2000 and 2022, a total of 103.37 km<sup>2</sup> forest area was transformed into impervious surface. These transformations were outstanding from 2015 to 2022. The retarded conversions from forests to impervious surfaces showed that the slope of the curve decreased despite some fluctuations. Under the rapid urbanization of Hangzhou City, evergreen broadleaved forests contributed the most area among the three forest types over the 23 years; however, the occupation of the other forest types by impervious surfaces varied annually. The percentages of evergreen needle-leaved forests were larger than deciduous broadleaved forests, except from 2009 to 2010 and 2011 to 2012. During these periods, the changes from evergreen needle-leaved forests to impervious surfaces did not appear in Hangzhou City. The conversions from deciduous broadleaved forests to impervious surfaces occurred in 10 years among 22 periods, mostly outstanding during the 2011 to 2012 period. The remarkable contributions of evergreen broadleaved and needle-leaved forests occurred during the 2002 to 2003 and 2001 to 2002 periods, respectively.

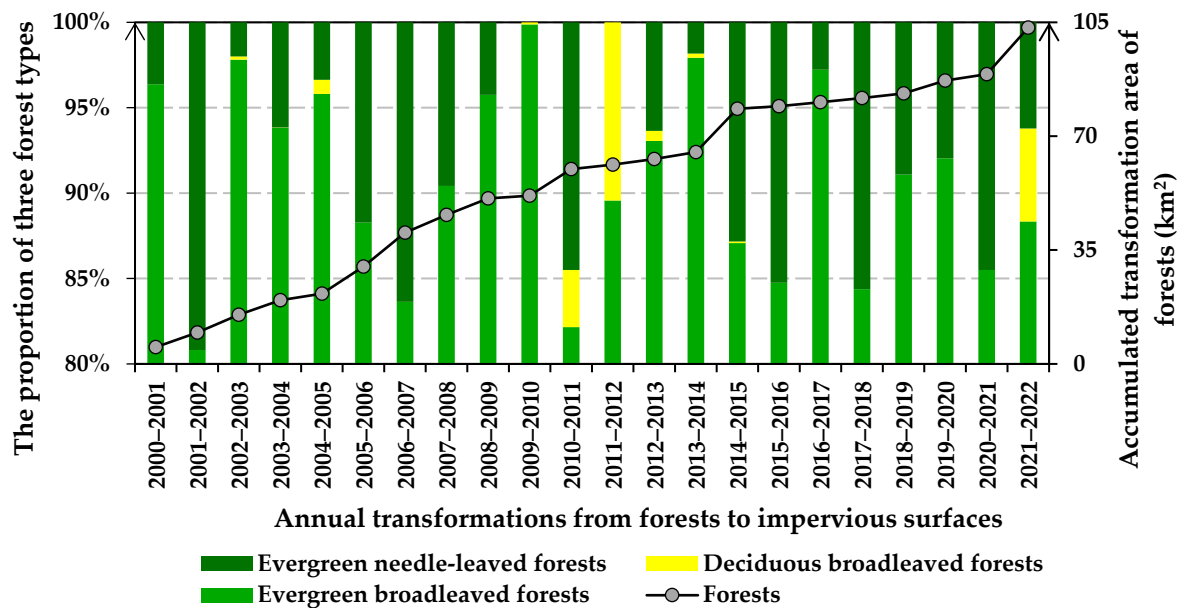
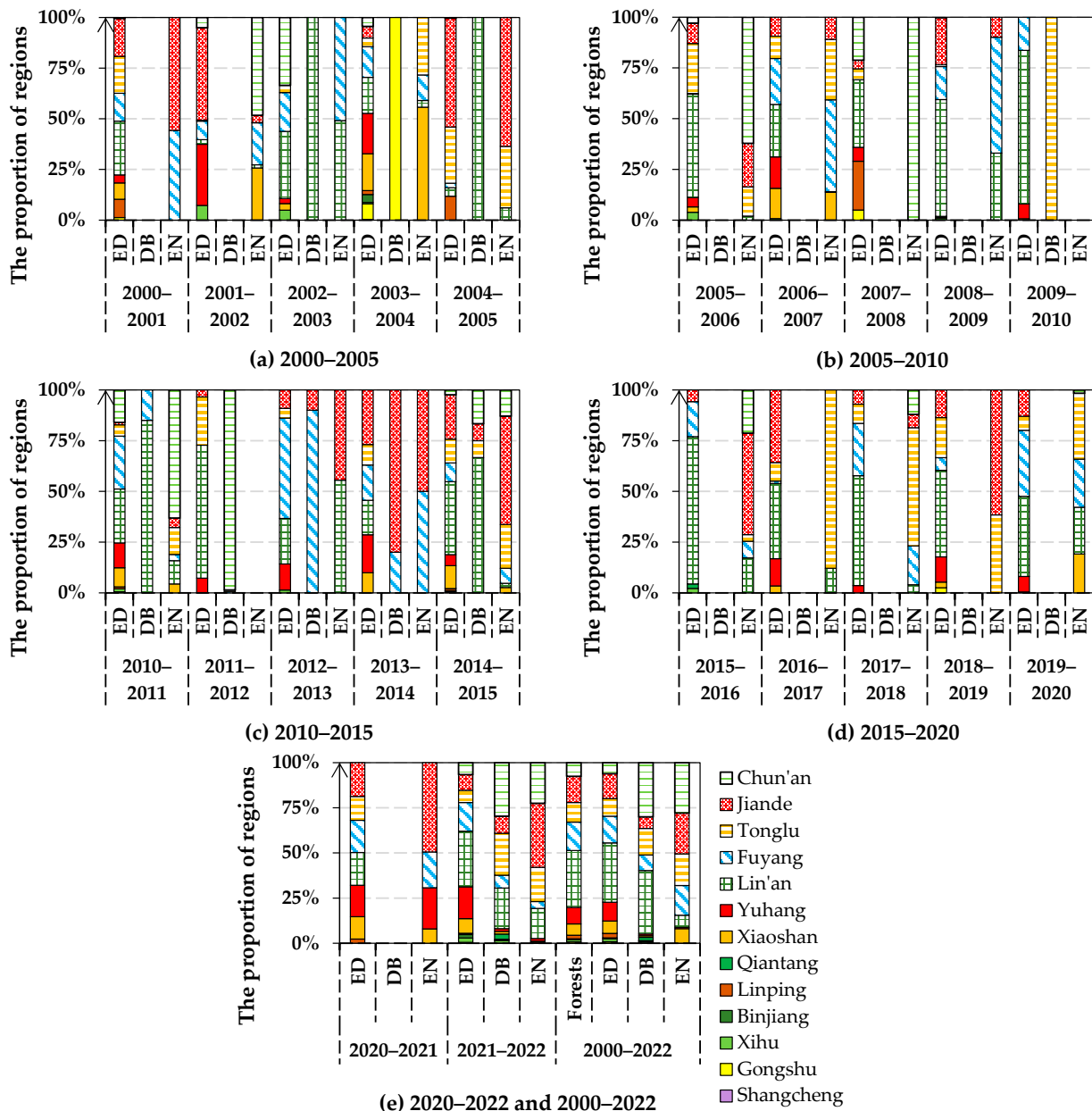


Figure 5. Annual transformations from forests to impervious surfaces.

The annual spatial differences of forest transformations to impervious surfaces among regions were quantified via spatial analysis and summarized in Figure 6. Within the first 5 years, the conversions from evergreen broadleaved forests to impervious surfaces were mainly located in Lin'an, Jiande, and Fuyang (Figure 6a). The occupation of deciduous broadleaved forests by impervious surfaces only occurred in Jiande and Gongshu from 2002 to 2005. Evergreen needle-leaved forests in Chun'an, Xiaoshan, and Fuyang represented most of the conversions to impervious surfaces. The spatial variations increased over the next five years (Figure 6b). Evergreen broadleaved forests in Lin'an accounted for the majority of conversions to impervious surfaces during the 2005 to 2010 period. The transformation from deciduous broadleaved forests to impervious surfaces only occurred in Tonglu from 2009 to 2010. Evergreen needle-leaved forests in Chun'an and Fuyang accounted for more than half the conversions to impervious surfaces. Regarding the period from 2010 to 2015, Lin'an still led with the proportion of conversions from evergreen broadleaved forests to impervious surfaces, followed by Fuyang and Jiande (Figure 6c). During this period, deciduous broadleaved forests transformed to impervious surfaces increased and chiefly appeared in Lin'an. The sum proportion of evergreen needle-leaved forests in Jiande, Chun'an, and Tonglu represented the majority. Between 2015 and 2020, the conversions from evergreen broadleaved forests to impervious surfaces were similar to those during the 2000 to 2005 period (Figure 6d). Within these five years, urban expansion did not occupy deciduous broadleaved forests. Evergreen needle-leaved forests in Tonglu and Jiande had the majority of conversions to impervious surfaces. Over the past two years, Lin'an, Yuhang, and Fuyang contributed the most deciduous broadleaved forests to urbanization (Figure 6e). The transformations from deciduous broadleaved forests to impervious surfaces widely occurred across Hangzhou City from 2020 to 2022, mostly in Chun'an, Tonglu, and Lin'an. The changes from evergreen needle-leaved forests to impervious surfaces were mainly in Jiande and Chun'an. Overall, over the 23 years studied, Lin'an, Fuyang, and Jiande were the top three regions in which the rapid expansion of impervious surfaces occupied great areas of forests. Evergreen broadleaved forests and whole forests converted alike. The temporal frequency of changes from evergreen needle-leaved forests to impervious surfaces was higher than that of conversions from deciduous broadleaved forests. Conversions from deciduous broadleaved forests to impervious surfaces displayed stronger spatial heterogeneity across Hangzhou City than those from evergreen needle-leaved forests. Changes from deciduous broadleaved forests to impervious surfaces were

mainly located in Lin'an and Chun'an, and those from evergreen needle-leaved forests were chiefly in Chun'an and Jiande.



**Figure 6.** Temporal dynamics of spatial variations of conversions from different forest types to impervious surfaces summarized according to regions, covering the following periods: 2000 to 2005 (a), 2005 to 2010 (b), 2010 to 2015 (c), 2015 to 2020 (d), 2020 to 2022, and 2000 to 2022 (e).

### 3.3. Relations of Spatiotemporal Patterns between Various Types of Forests and Impervious Surfaces

The area-weighted centroids of forests and impervious surfaces were determined via spatial analysis and are depicted in Figure 7. Over 23 years, these five groups of centroids from different land-use types had varying degrees of movement; however, they were still within the same region. Indeed, 23 centroids of impervious surfaces were in Xihu, and those of forests and evergreen broadleaved forests were in Tonglu. On the other hand, centroids of deciduous broadleaved and evergreen needle-leaved forests were located in Chun'an. Among the five groups, centroids of impervious surfaces moved the most, followed by evergreen needle-leaved forests, evergreen broadleaved forests, forests,

and deciduous broadleaved forests. Regarding the centroid movements of the forests, evergreen broadleaved and needle-leaved forests resembled one another. These three groups of centroids all moved towards the southwest. The centroids of impervious surfaces and deciduous broadleaved forests had more complex annual shifts. It was shown that the impervious surface centroid firstly moved southwestward and then shifted to the northwest. After that, the centroid of impervious surfaces went to the southwest again and finally toward the north. The deciduous broadleaved forests centroid headed for the southwest and then went to the north. Subsequently, the centroid of deciduous broadleaved forests moved to the southeast, with a final turn northwestward.

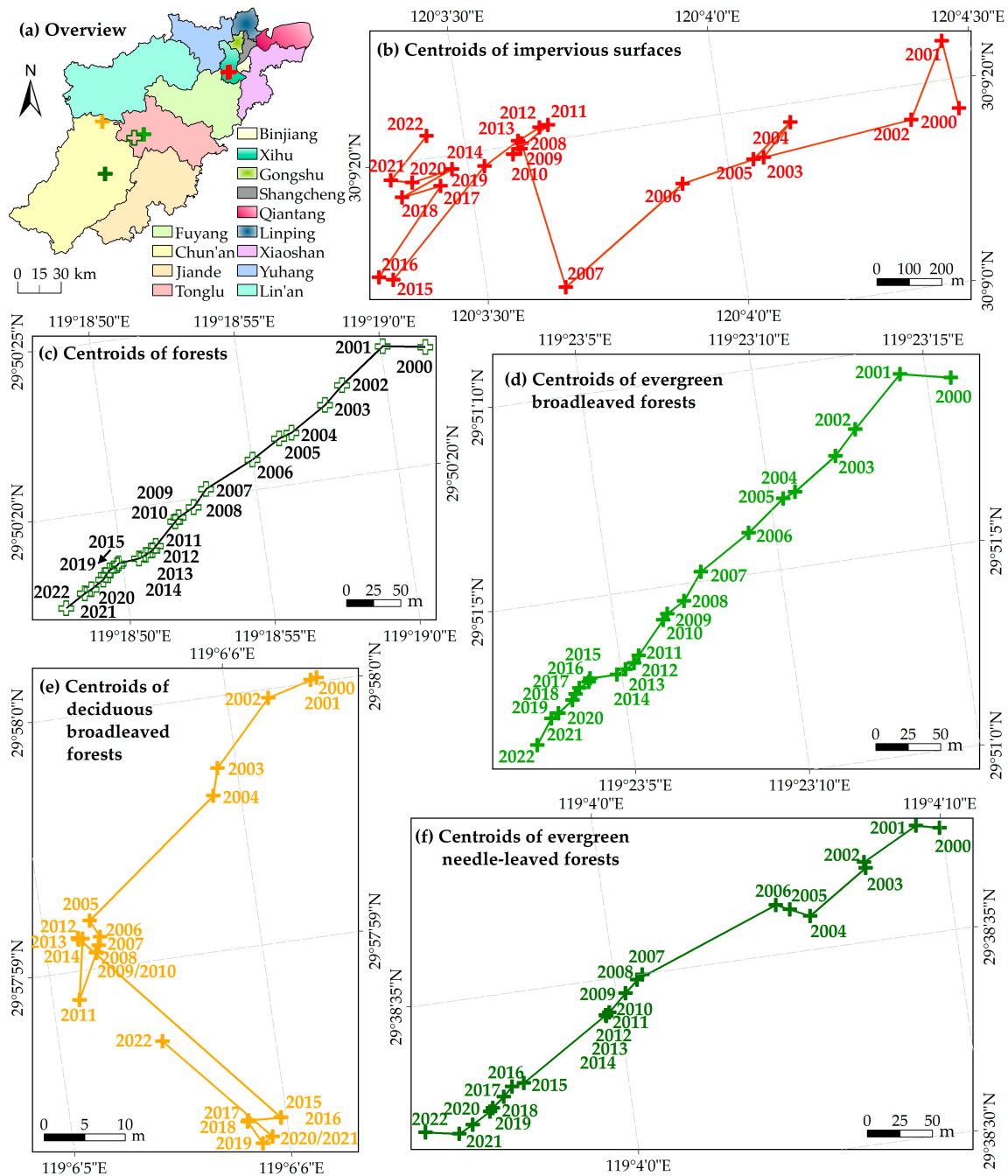


**Figure 7.** Overview of centroid locations (a) with annual centroid movements of impervious surfaces (b), forests (c), evergreen broadleaved forests (d), deciduous broadleaved forests (e), and evergreen needle-leaved forests (f).

The landscape pattern indexes at the class level were calculated and are summarized in Figure 8. The PLAND values of all forests reduced, whereas those of impervious surfaces increased, and these changes slowed down over 23 years (Figure 8a). Evergreen broadleaved forests had the largest PLAND values, and deciduous broadleaved forests had the smallest. The PLAND value variation for impervious surfaces was the greatest at 29.34%, followed by evergreen broadleaved at 1.39%, evergreen needle-leaved, and deciduous broadleaved forests. The LPI annual changes in forests and impervious surfaces were approximate to PLAND (Figure 8b). However, the value ranking was different, as evergreen needle-leaved forests had the minimum. The results demonstrated that the FFRAC\_AM values for all forests lowered slightly, with the largest decline being in evergreen broadleaved forests, while the values of impervious surfaces increased, then slowly decreased (Figure 8c). The order of the FFRAC\_AM of forests and impervious surfaces was same as that of the LPI values. All LSI values decreased, and the order of the forests and impervious surfaces by shrinkage degree was the same as that of the LPI (Figure 8d). Nevertheless, evergreen needle-leaved forests had the largest LSI, and impervious surfaces had the minimum. The PD values of evergreen broadleaved and deciduous broadleaved forests showed a slight increase (Figure 8e). The PD decrease for impervious surfaces was relatively remarkable, at 5.7% compared to that of evergreen needle-leaved forests over the 23 years studied. Evergreen needle-leaved forests had the greatest PD, followed by deciduous broadleaved and evergreen broadleaved forests, and impervious surfaces demonstrated the lowest PD values. The SPLIT values for all forest types increased, whereas those of impervious surfaces lowered (Figure 8f). Evergreen needle-leaved forests had the maximum, followed by deciduous broadleaved forests and impervious surfaces. The SPLIT of evergreen broadleaved forests was the smallest. The order of the change degree from highest to lowest values was as follows: impervious surfaces, evergreen broadleaved, deciduous broadleaved, and evergreen needle-leaved forests; this was also the same for LPI values.

The spatiotemporal pattern relationship between the forest types and impervious surfaces was highlighted by the relevance of centroid movements and class-level indexes. The centroid movements of the forest types and impervious surfaces were broadly consistent with a southwestward tendency from 2000 to 2022. This consistency indicated the spatial relationships between the reduction in forests and the soar in impervious surfaces. The opposite changes of index values of the forest types and impervious surfaces, such as that of PLAND, LPI, and SPLIT, elucidated that all types of forests lost area and became fragmented due to the rapid expansion of impervious surfaces. Although the PD values of evergreen needle-leaved forests slightly lowered due to the amount of area lost, the forest fragmentation quantified via PD aligned with the aggregation of impervious surface expansion described by PD and LSI. This situation was tardier within the most recent years of this study, as depicted by the slower dynamics shown in Figure 8, which was also demonstrated by the coherence between FRAC\_AM changes of forest types and impervious surfaces after 2012.

The landscape-level indexes were computed and are shown in Figure 9. The change trends for FRAC\_AM, LSI, SPLIT, CONTAG, SHDI, and SHEI of forests and the entire Hangzhou City were similar. Nonetheless, regarding ED, LPI, and PD, forests and Hangzhou City displayed opposite variations. Moreover, the dynamics of all indexes became tardive within the 23 years of the study. The chief indexes of the forests had increments, excluding FRAC\_AM, LSI, and CONTAG; on the other hand, those of Hangzhou City decreased, except for SPLIT, SHDI, and SHEI. The forest pattern dynamics, due to the urbanization of Hangzhou City, were depicted by the relationship between centroid movements and landscape-level indexes. Forests showed close spatiotemporal patterns to evergreen broadleaved forests, which elucidated the southwest-oriented decline in forests over 23 years. As demonstrated by the value dynamics of ED and PD, forests became fragmented despite the stronger aggregation of impervious surfaces. The value changes in LPI, SHDI, and SHEI indicated that the area differences in forest patches were enhanced, while the dominance among forest types declined within the increasing homogeneous

landscape. The complexity and heterogeneity of natural landscapes reduced with a slower speed, displayed by the decreasing FRAC\_AM and LSI. The booming SPLIT and CONTAG values elucidated the lessening adjacencies.

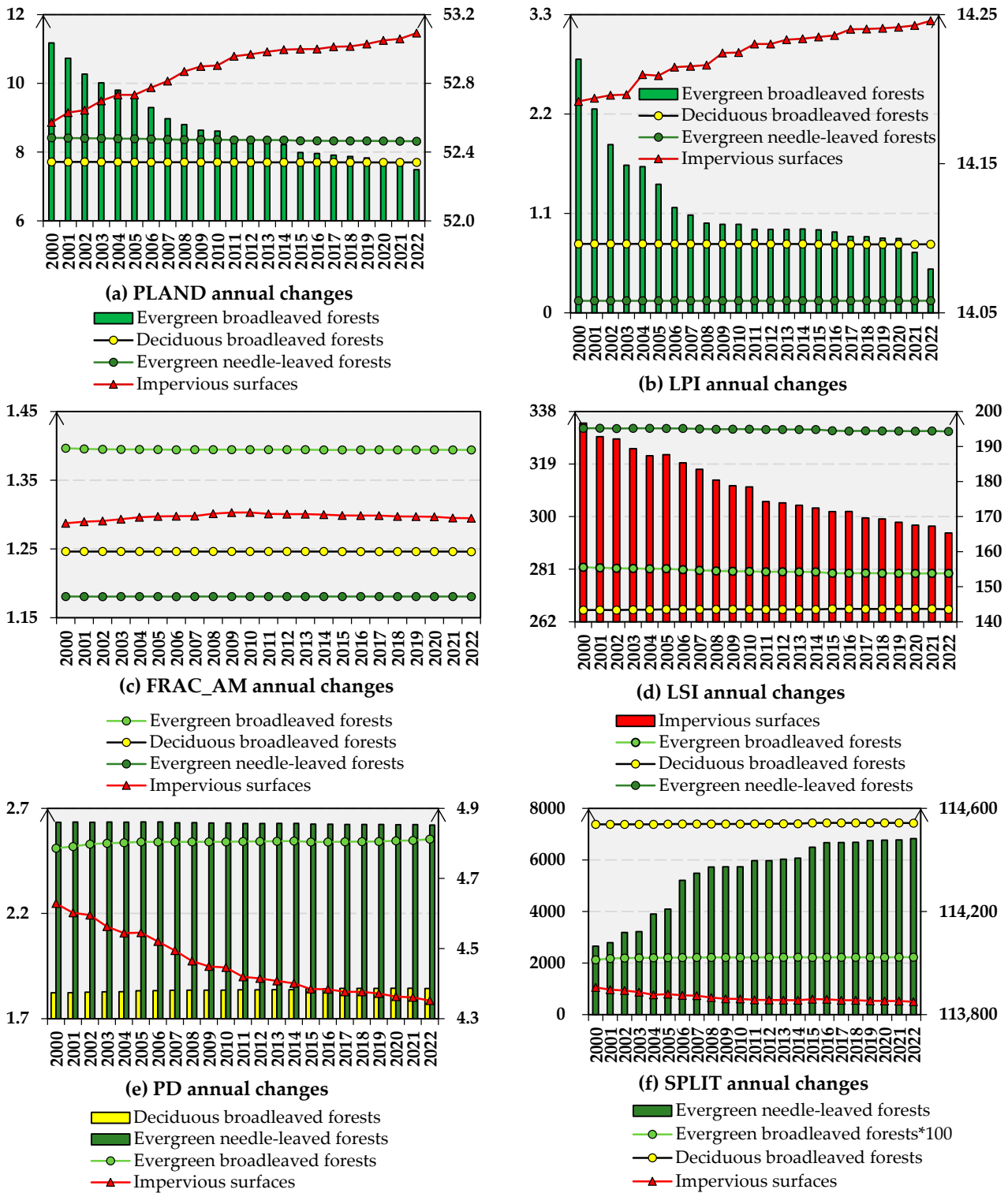


**Figure 8.** Annual values of landscape pattern indexes of forests and impervious surfaces at the class level. The vertical coordinate presents the values of the lines, and the sub-vertical coordinate is for the bars.

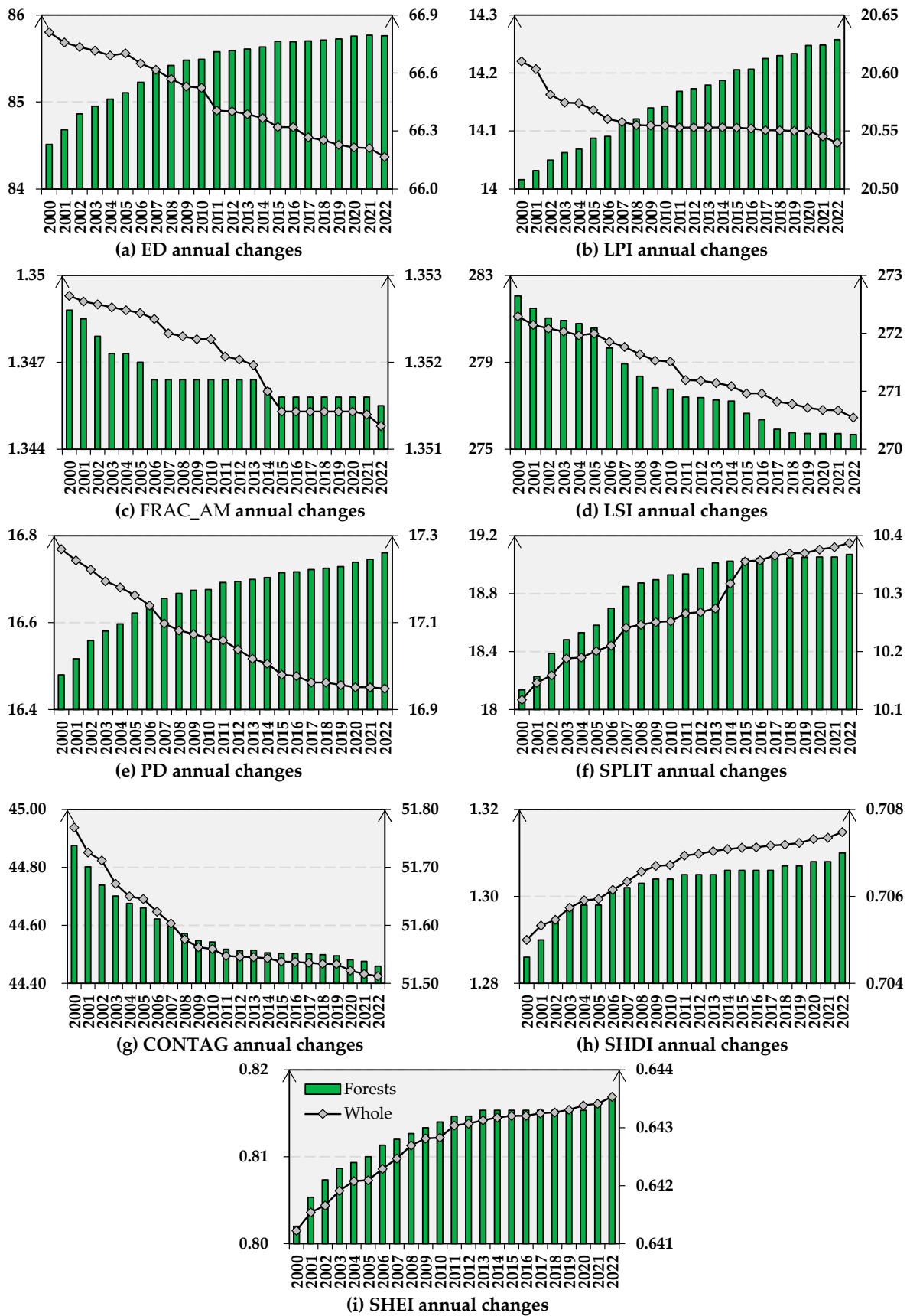


**Figure 9.** Annual values of the landscape pattern indexes for forests and the whole study area at the landscape level.

## 4. Discussion

### 4.1. Spatiotemporal Patterns of Various Types of Forests

The spatiotemporal differences of the three forest types were determined via the annual summary of area and distribution, as shown in Figure 4, and they were depicted by the centroid movements shown in Figure 7, as well as the indexes in Figure 8. As the majority, evergreen broadleaved forests generally dominated the spatiotemporal patterns of forests in Hangzhou City. The southwest-oriented decline in evergreen broadleaved forests largely resulted in lost forest area in Hangzhou City. Although the southwest region, i.e., Chun'an, Lin'an, and Jiande, mostly encompassed evergreen broadleaved forests, the forest reduction in these regions was relative remarkable. Moreover, evergreen broadleaved forests showed the largest shrinkage among the three types, which greatly contributed to the dominance decrease based on the dynamics of the landscape indexes. Despite the great loss, evergreen broadleaved forests still dominated among the three types, with the best adjacency and minimal fragmentation. Deciduous broadleaved forests shrunk the least and also covered the smallest area, mainly located in the northwestern marginal regions of Hangzhou City. Nonetheless, change directions were the most complex in deciduous broadleaved forests among the three forest types. Though the overall direction was similar to other forests, which was southwestwards, the annual changes were quite varied after 2011. According to landscape indexes, deciduous broadleaved forests maintained an average level of fragmentation but had the most complex shape among the three forest types. As the second-largest cover type, the proportion of evergreen needle-leaved forests changed the least among the three types, but it had the highest fragmentation and worst adjacency. The main distribution regions and change direction of evergreen needle-leaved forests were approximate to evergreen broadleaved forests; however, western-oriented loss was more outstanding among evergreen needle-leaved forests.

The temporal patterns for all forests generally displayed slower variations. The area changes were highlighted during the 2001 to 2002 period for evergreen broadleaved forests, 2004 to 2005 for deciduous broadleaved forests, and 2014 to 2015 for evergreen needle-leaved forests. These area losses had southwest orientation based on centroid movements. Regarding variations in landscape indexes, apart from PLAND and LSI, evergreen broadleaved forests had the greatest temporal dynamics among the three forest types, followed by deciduous broadleaved and evergreen needle-leaved forests. Evergreen broadleaved forests also demonstrated the highest temporal variations in PLAND and LSI values. On the other hand, deciduous broadleaved forests showed fewer temporal dynamics for PLAND and LSI values than evergreen needle-leaved forests. These differences resulted from area changes in evergreen needle-leaved forests being bigger than that of deciduous broadleaved forests. It was revealed that the fragmentation degree of evergreen broadleaved forests increased the most, and the adjacency loss was the greatest. Simultaneously, it was indicated that evergreen needle-leaved forests had the least changes in fragmentation and adjacency; this was also the reason why forests became homogeneous at the landscape level.

In summary, this study identified and compared the spatiotemporally explicit patterns of evergreen broadleaved, deciduous broadleaved, and evergreen needle-leaved forests. These results explain the forest dynamics and can support forest management in Hangzhou City at a finer spatiotemporal scale.

### 4.2. Spatiotemporal Responses of Different Types of Forests to Rapid Urbanization

The spatiotemporal responses of the three forest types to rapid urbanization during the 2000 to 2022 period were inferred by the annual transformation (Figures 5 and 6), and they were described via the comparison of centroid movements (Figure 7) and index changes (Figure 8). These results all indicated that evergreen broadleaved forests annually contributed the largest area, suffering the most consequence from rapid urbanization widely across Hangzhou City, especially in Li'an Fuyang and Jiande. It also resulted in the largest increasing degree of fragmentation of evergreen broadleaved forests, as well as the

greatest loss of adjacency as a response to the enhancing aggregation and dominance of impervious surfaces. Contrastingly, deciduous broadleaved forests lost the least area to impervious surface expansion, mainly in Lin'an and Chun'an, except for the two periods from 2009 to 2010 and 2011 to 2012. The response of evergreen needle-leaved forests to urbanization was similar to that of evergreen broadleaved forests, as shown in Figure 7. On the other hand, the transformations of evergreen needle-leaved forests to impervious surfaces had more spatiotemporal variations than those of evergreen broadleaved forests, mainly occurring in Chun'an and Jiande.

The general directions of centroid movements of forests and impervious surfaces were consistent, which was revealed through the southwestward shrinkage response of forests to urban expansion. At the same time, the annual directions of forest centroid movements shown in Figure 7 were partly in line with the location of the major transformation regions summarized in Figure 6. Additionally, this consistency was enhanced when relating centroid movements to transformation over five-year intervals. It was uncovered that the expansion of impervious surfaces was the primary reason underlying forest dynamics, and these responses were more outstanding at certain time intervals. Although the transformation from forests to impervious surfaces was relatively remarkable in the years between 2015 and 2022, the overall response of forests to rapid urbanization lessened with some fluctuations over 23 years. Moreover, these response changes had time coincidences with adjustments of administrative divisions of Hangzhou City. In 2001, Xiaoshan and Yuhang were incorporated into Hangzhou City [48], when the centroids of forests moved southwards (Figure 7). From 2001 to 2012, remarkable conversions from evergreen broadleaved forests to impervious surfaces in Yuhang and those from evergreen needle-leaved forests in Xiaoshan were observed, as outlined in Figure 6a. At the end of 2014, Fuyang was merged into the city [48]; meanwhile, forests in Fuyang presented substantial transformations to impervious surfaces during the 2012 to 2014 period (Figure 6c). Furthermore, the centroids of forests and impervious surfaces also showed long-distance movements from 2014 to 2015. Then, Lin'an was included as a region of Hangzhou City in 2017, and Qiantang was established in 2019 [49,50]. Through the above-described adjustments, Hangzhou City entered the "Qiantang Era" from the "Xihu Era" and became polycentric [51], which also elucidated the reason behind the transformation of forests to impervious surfaces, mainly appearing in newly built urban regions (Figure 6d). In 2021, these administrative divisions were greatly adjusted, as shown in Figure 1 [52], which was in line with the outstanding transformations of forests to impervious surfaces (Figure 5).

In short, the adjustments of administrative divisions in Hangzhou City largely explained the spatiotemporal responses of forests to urbanization. Forests contributed a large amount of area and adjacency to the development of Hangzhou City, particularly evergreen broadleaved forests, whereas the degradation of forests due to urbanization slowed down.

#### 4.3. Uncertainty and Urban Forest Managements

The uncertainty of this study was generated and controlled among the annual spatial distribution mapping of various forest types, as well as by quantifying the spatiotemporal transformation and analyzing the spatiotemporal patterns. In order to accomplish the change analysis effectively and avoid pseudo changes, object-based backdating classification was applied that could produce results quicker, more accurately, and consistently with previous mapping efforts and existing data. Alongside that, all good-quality Landsat images were adopted to acquire mosaic images of the summer and winter images adopted in this study to reduce the uncertainty of annual forest-type mapping. Despite being limited by the ground-truth field samples, the accuracy of forest-type maps remained uncertain and can be improved in follow-up works by integrating high-quality ground-observed data. The occupation of forests by impervious surfaces was annually quantified using the transfer matrix and summarized according to regions to provide multiple spatiotemporal scales to reduce uncertainty. To comprehensively determine the spatiotemporal patterns of forests under rapid urbanization, centroid movements that combined landscape indexes at two

levels were used. The improvement of this study is particularly reflected in the finer temporal resolution and class-level analysis of the forests. Through the above three steps, the response of forest types to the rapid expansion of impervious surfaces was quantified and integrated from area changes and spatial change direction, as well as landscape patterns of dominance, fragmentation, adjacency, and homogeneity. The multiple spatiotemporal scales in this study revealed that the optimal time interval and spatial unit should be explored in more depth in further works.

Based on the results and above discussions, urban development planning, including adjustments to administrative divisions, deeply affected forests. For sustainable urban development, measures based on the spatiotemporal responses of forests to urbanization should be implemented. Owing to the strict protection of ecological environments in Chun'an, the land-use of Chun'an was quite stable over the 23 years of the study. However, impervious surfaces still occupied forests due to tourism developments in this region [43,53]. The fragmentation and adjacency of forests in the western regions of Hangzhou City, i.e., Chun'an, Li'an, and Jiande, where evergreen broadleaved and evergreen needle-leaved forests extensively grew, should be paid close attention to. A green ecological corridor can be constructed in these regions [54]. Southwestern regions, such as Tonglu and Fuyang, should also be strictly controlled for transformations from forests to impervious surfaces.

In conclusion, this study considered the uncertainty from each step and advanced a Landsat-based methodology at a finer spatiotemporal scale to explicitly understand forest changes under high-speed urbanization. Certain measures should be taken to control forest transformations and improve the problems of fragmentation and adjacency loss.

## 5. Conclusions

To delineate explicitly spatiotemporal response of forests at a type scale to the rapid expansion of impervious surfaces, this pioneering study put forward a methodology using object-based backdating classification, transfer matrix, area-weighted centroids, and landscape pattern indexes based on the GLC\_FCS30 product and Landsat imagery during the period of 2000–2022. The following results were observed:

- (1) Forests were mainly located in the southwest and decreased in area from 11,660.69 to 11,516.15 km<sup>2</sup>, with the most rapid shrinkage occurring in the first ten years of the study, especially between 2006 and 2007. Evergreen broadleaved forests occupied the largest area and had the greatest decrease ratio among the three forest types over 23 years, followed by evergreen needle-leaved and deciduous broadleaved forests. Evergreen broadleaved forests mainly grew in Chun'an, Li'an, and Jiande, while deciduous broadleaved forests were mainly in Li'an, Chun'an, and Tonglu. The majority of evergreen needle-leaf forests were in Chun'an, Jiande, and Lin'an.
- (2) A total of 103.37 km<sup>2</sup> of forest area was transformed to impervious surfaces. Among the three types, evergreen broadleaved forests annually contributed the largest area widely across Hangzhou City, especially in Li'an Fuyang and Jiande. Contrastingly, deciduous broadleaved forests lost the least area to impervious surface expansion, with the strongest spatial heterogeneity, mainly in Lin'an and Chun'an, except from 2009 to 2010 and 2011 to 2012. The temporal frequency of the changes from evergreen needle-leaved forests to impervious surfaces was higher than that of conversions from deciduous broadleaved forests, which mainly occurred in Chun'an and Jiande.
- (3) Forests lost remarkable area and adjacency due to the development of Hangzhou City, while this southwestward shrinkage slowed down over 23 years. Evergreen broadleaved forests annually contributed the largest area widely across Hangzhou City, which also resulted in the largest increasing degree of fragmentation. The response of evergreen needle-leaved forests to the enhancing aggregation and dominance of impervious surfaces was similar to that of evergreen broadleaved forests. On the other hand, evergreen needle-leaved forests showed the least change in fragmentation and adjacency. This also led to the increasing homogeneity of forests at the landscape level due to the expansion of impervious surfaces.

Forest management strategies were discussed based on the above findings. This study provides results at multiple spatiotemporal scales; however, optimal time intervals and spatial units should be explored in more depth in future works.

**Supplementary Materials:** The following supporting information can be downloaded at: <https://www.mdpi.com/article/10.3390/f15010044/s1>, Table S1: List of Landsat images used to create a mosaic for mapping forest types and impervious surfaces.

**Author Contributions:** Y.Z.: data curation, formal analysis, investigation, methodology, validation, visualization, writing—original draft. J.Z.: data curation, formal analysis, investigation, methodology, validation, visualization. M.L.: investigation, software, validation, writing—review and editing. W.M.: investigation, software, validation, writing—review and editing. L.C.: conceptualization, funding acquisition, supervision, project administration, resources, writing—original draft. All authors have read and agreed to the published version of the manuscript.

**Funding:** This research was funded by the National Natural Science Foundation of China (No. 42101323), Natural Science Foundation of Zhejiang Province, China (No. LQ22D010001), and Scientific Research Foundation for Scholars of HZNU (No. 4085C50220204092).

**Data Availability Statement:** The AW3D30 product and composited Landsat images were downloaded from the Google Earth Engine (<http://code.earthengine.google.com>, accessed on 1 February 2023). The GLC\_FCS30 products were downloaded from the Big Earth Data Science Engineering Program (CASEarth) (<https://data.casearth.cn/>, accessed on 4 January 2022).

**Acknowledgments:** The authors appreciate the National Earth System Science Data Center, National Science and Technology Infrastructure of China (<http://www.geodata.cn>, accessed on 4 April 2023).

**Conflicts of Interest:** The authors declare no conflicts of interest.

## References

1. Wang, J.; Chen, Y.; Liao, W.; He, G.; Tett, S.F.B.; Yan, Z.; Zhai, P.; Feng, J.; Ma, W.; Huang, C.; et al. Anthropogenic emissions and urbanization increase risk of compound hot extremes in cities. *Nat. Clim. Chang.* **2021**, *11*, 1084–1089. [[CrossRef](#)]
2. Wang, K.; Onodera, S.; Saito, M.; Shimizu, Y. Long-term variations in water balance by increase in percent imperviousness of urban regions. *J. Hydrol.* **2021**, *602*, 126767. [[CrossRef](#)]
3. Endreny, T.A. Strategically growing the urban forest will improve our world. *Nat. Commun.* **2018**, *9*, 1160. [[CrossRef](#)]
4. Lund, N.S.V.; Borup, M.; Madsen, H.; Mark, O.; Arnbjerg-Nielsen, K.; Mikkelsen, P.S. Integrated stormwater inflow control for sewers and green structures in urban landscapes. *Nat. Sustain.* **2019**, *2*, 1003–1010. [[CrossRef](#)]
5. Yu, W.; Shi, J.; Fang, Y.; Xiang, A.; Li, X.; Hu, C.; Ma, M. Exploration of urbanization characteristics and their effect on the urban thermal environment in Chengdu, China. *Build. Environ.* **2022**, *219*, 109150. [[CrossRef](#)]
6. Hegetschweiler, T.; Wartmann, F.M.; Dubernet, I.; Fischer, C.; Hunziker, M. Urban forest usage and perception of ecosystem services—A comparison between teenagers and adults. *Urban For. Urban Green.* **2022**, *74*, 127624. [[CrossRef](#)]
7. Turlej, K.; Ozdogan, M.; Radeloff, V.C. Mapping forest types over large areas with Landsat imagery partially affected by clouds and SLC gaps. *Int. J. Appl. Earth Obs. Geoinf.* **2022**, *107*, 102689. [[CrossRef](#)]
8. Pregitzer, C.C.; Charlop-Powers, S.; Bibbo, S.; Forgione, H.M.; Gunther, B.; Hallett, R.A.; Bradford, M.A. A city-scale assessment reveals that native forest types and overstory species dominate New York City forests. *Ecol. Appl.* **2019**, *29*, e01819. [[CrossRef](#)]
9. Zhang, D.; Zheng, H.; He, X.; Ren, Z.; Zhai, C.; Yu, X.; Mao, Z.; Wang, P. Effects of forest type and urbanization on species composition and diversity of urban forest in Changchun, Northeast China. *Urban Ecosyst.* **2016**, *19*, 455–473. [[CrossRef](#)]
10. Pettorelli, N.; Laurance, W.F.; O'Brien, T.G.; Wegmann, M.; Nagendra, H.; Turner, W. Satellite remote sensing for applied ecologists: Opportunities and challenges. *J. Appl. Ecol.* **2014**, *51*, 839–848. [[CrossRef](#)]
11. Shin, N.; Katsumata, C.; Miura, T.; Tsutsumida, N.; Ichie, T.; Kotani, A.; Nakagawa, M.; Khoo, K.L.; Kobayashi, H.; Kumagai, T.; et al. Perspective: Improving the accuracy of plant phenology observations and land-cover and land-use detection by optical satellite remote-sensing in the Asian tropics. *Front. For. Glob. Chang.* **2023**, *6*, 1106723. [[CrossRef](#)]
12. Banskota, A.; Kayastha, N.; Falkowski, M.J.; Wulder, M.A.; Froese, R.E.; White, J.C. Forest monitoring using Landsat time series data: A review. *Can. J. Remote Sens.* **2014**, *40*, 362–384. [[CrossRef](#)]
13. Cai, Y.; Shi, Q.; Xu, X.; Liu, X. A novel approach towards continuous monitoring of forest change dynamics in fragmented landscapes using time series Landsat imagery. *Int. J. Appl. Earth Obs. Geoinf.* **2023**, *118*, 103226. [[CrossRef](#)]
14. Nguyen, T.H.; Jones, S.D.; Soto-Berelov, M.; Haywood, A.; Hislop, S. A spatial and temporal analysis of forest dynamics using Landsat time-series. *Remote Sens. Environ.* **2018**, *217*, 461–475. [[CrossRef](#)]
15. Cheng, K.; Wang, J.; Yan, X. Mapping Forest Types in China with 10 m Resolution Based on Spectral–Spatial–Temporal Features. *Remote Sens.* **2021**, *13*, 973. [[CrossRef](#)]

16. Decuyper, M.; Chávez, R.O.; Lohbeck, M.; Lastra, J.A.; Tsendbazar, N.; Hackländer, J.; Herold, M.; Vågen, T.G. Continuous monitoring of forest change dynamics with satellite time series. *Remote Sens. Environ.* **2022**, *269*, 112829. [[CrossRef](#)]
17. Aghababaei, M.; Ebrahimi, A.; Naghipour, A.A.; Asadi, E.; Verrelst, J. Vegetation Types Mapping Using Multi-Temporal Landsat Images in the Google Earth Engine Platform. *Remote Sens.* **2021**, *13*, 4683. [[CrossRef](#)]
18. Zhang, X.; Liu, L.; Chen, X.; Gao, Y.; Xie, S.; Mi, J. GLC\_FCS30: Global land-cover product with fine classification system at 30 m using time-series Landsat imagery. *Earth Syst. Sci. Data* **2021**, *13*, 2753–2776. [[CrossRef](#)]
19. Ioki, K.; James, D.; Phua, M.-H.; Tsuyuki, S.; Imai, N. Recovery of tree community composition across different types of anthropogenic disturbances and characterization of their effect using Landsat time series in Bornean tropical montane forest. *Biol. Conserv.* **2022**, *267*, 109489. [[CrossRef](#)]
20. Akaraci, S.; Feng, X.; Suesse, T.; Jalaludin, B.; Astell-Burt, T. Associations between green space, air pollution and birthweight in Sydney Metropolitan Area, Australia. *Urban For. Urban Green.* **2022**, *76*, 127726. [[CrossRef](#)]
21. Liu, S.; Zhang, X.; Feng, Y.; Xie, H.; Jiang, L.; Lei, Z. Spatiotemporal Dynamics of Urban Green Space Influenced by Rapid Urbanization and Land Use Policies in Shanghai. *Forests* **2021**, *12*, 476. [[CrossRef](#)]
22. Mansour, S.; Nasiri, N.A.; Abulibdeh, A.; Ramadan, E. Spatial disparity patterns of green spaces and buildings in arid urban areas. *Buid. Environ.* **2022**, *208*, 108588. [[CrossRef](#)]
23. Shen, W.; Mao, X.; He, J.; Dong, J.; Huang, C.; Li, M. Understanding current and future fragmentation dynamics of urban forest cover in the Nanjing Laoshan Region of Jiangsu, China. *Remote Sens.* **2020**, *12*, 155. [[CrossRef](#)]
24. Kowe, P.; Mutanga, O.; Odindi, J.; Dube, T. Effect of landscape pattern and spatial configuration of vegetation patches on urban warming and cooling in Harare metropolitan city, Zimbabwe. *GISci. Remote Sens.* **2021**, *58*, 261–280. [[CrossRef](#)]
25. Yang, K.; Sun, W.; Luo, Y.; Zhao, L. Impact of urban expansion on vegetation: The case of China (2000–2018). *J. Environ. Manag.* **2021**, *291*, 112598. [[CrossRef](#)]
26. Escobedo, F.J.; Palmas-Perez, S.; Dobbs, C.; Gezan, S.; Hernandez, J. Spatio-Temporal Changes in Structure for a Mediterranean Urban Forest: Santiago, Chile 2002 to 2014. *Forests* **2016**, *7*, 121. [[CrossRef](#)]
27. Li, L.; Zhan, W.; Ju, W.; Peñuelas, J.; Zhu, Z.; Peng, S.; Zhu, X.; Liu, Z.; Zhou, Y.; Li, J.; et al. Competition between biogeochemical drivers and land-cover changes determines urban greening or browning. *Remote Sens. Environ.* **2023**, *287*, 113481. [[CrossRef](#)]
28. Nowak, D.J.; Greenfield, E.J. The increase of impervious cover and decrease of tree cover within urban areas globally (2012–2017). *Urban For. Urban Green.* **2020**, *49*, 126638. [[CrossRef](#)]
29. Chen, Y.; Xu, Z.; Byrne, J.; Xu, T.; Wang, S.; Wu, J. Can smaller parks limit green gentrification? Insights from Hangzhou, China. *Urban For. Urban Green.* **2021**, *59*, 127009. [[CrossRef](#)]
30. Li, X.; Guo, J.; Qi, S. Forestland landscape change induced spatiotemporal dynamics of subtropical urban forest ecosystem services value in forested region of China: A case of Hangzhou city. *Environ. Res.* **2021**, *193*, 110618. [[CrossRef](#)]
31. Statistical Bulletin of Hangzhou National Economic and Social Development in 2022. Available online: [http://tjj.hangzhou.gov.cn/art/2023/3/20/art\\_1229279682\\_4149703.html](http://tjj.hangzhou.gov.cn/art/2023/3/20/art_1229279682_4149703.html) (accessed on 5 October 2023).
32. Chen, L.; Zhou, B.; Man, W.; Liu, M. Landsat-Based Monitoring of the Heat Effects of Urbanization Directions and Types in Hangzhou City from 2000 to 2020. *Remote Sens.* **2021**, *13*, 4268. [[CrossRef](#)]
33. Xiang, S.; Huang, L.; Zhou, M.; Shan, L.; Dong, B.; Wang, K. Dynamic analysis of correlation patterns between urban population and construction land at different administrative levels: The case of Hangzhou megacity. *Ecol. Indic.* **2023**, *154*, 110407. [[CrossRef](#)]
34. Jiao, J.; Wu, C.; Jiang, B.; Wang, Z.; Yuan, W.; Zhu, J.; Li, T.; Yang, S.; Yao, L. Negative Density Restricts the Coexistence and Spatial Distribution of Dominant Species in Subtropical Evergreen Broad-Leaved Forests in China. *Forests* **2022**, *13*, 1227. [[CrossRef](#)]
35. Shen, C.; Hou, H.; Zheng, Y.; Murayama, Y.; Wang, R.; Hu, T. Prediction of the future urban heat island intensity and distribution based on landscape composition and configuration: A case study in Hangzhou. *Sust. Cities Soc.* **2022**, *83*, 103992. [[CrossRef](#)]
36. Lu, H.; Li, F.; Yang, G.; Sun, W. Multi-scale impacts of 2D/3D urban building pattern in intra-annual thermal environment of Hangzhou, China. *Int. J. Appl. Earth Obs. Geoinf.* **2021**, *104*, 102558. [[CrossRef](#)]
37. Han, S.; Hou, H.; Estoque, R.C.; Zheng, Y.; Shen, C.; Murayama, Y.; Pan, J.; Wang, B.; Hu, T. Seasonal effects of urban morphology on land surface temperature in a three-dimensional perspective: A case study in Hangzhou, China. *Buid. Environ.* **2023**, *228*, 109913. [[CrossRef](#)]
38. Tian, P.; Li, J.; Cao, L.; Pu, R.; Gong, H.; Liu, Y.; Zhang, H.; Chen, H. Impacts of reclamation derived land use changes on ecosystem services in a typical gulf of eastern China: A case study of Hangzhou bay. *Ecol. Indic.* **2021**, *132*, 108259. [[CrossRef](#)]
39. Wang, Z.; Xu, L.; Shi, Y.; Ma, Q.; Wu, Y.; Lu, Z.; Mao, L.; Pang, E.; Zhang, Q. Impact of Land Use Change on Vegetation Carbon Storage During Rapid Urbanization: A Case Study of Hangzhou, China. *Chin. Geogr. Sci.* **2021**, *31*, 209–222. [[CrossRef](#)]
40. Meng, X.; Bao, Y.; Luo, C.; Zhang, X.; Liu, H. SOC content of global Mollisols at a 30 m spatial resolution from 1984 to 2021 generated by the novel ML-CNN prediction model. *Remote Sens. Environ.* **2024**, *300*, 113911. [[CrossRef](#)]
41. Wang, Y.; Chen, L. A hybrid approach for mapping salt marsh vegetation. In *Coastal and Marine Environments*, 2nd ed.; Wang, Y., Ed.; CRC Press: Boca Raton, FL, USA, 2020; pp. 299–306. [[CrossRef](#)]
42. Rafael, D.A.; Virginia, G.G.; José, V.; Oliver, V.; Eduardo, R.B. Land use/cover change analysis in the Mediterranean region: A regional case study of forest evolution in Castelló (Spain) over 50 years. *Land Use Pol.* **2022**, *114*, 105967. [[CrossRef](#)]
43. Shangguan, Y.; Li, X.; Lin, Y.; Deng, J.; Yu, L. Mapping spatial-temporal nationwide soybean planting area in Argentina using Google Earth Engine. *Int. J. Remote Sens.* **2022**, *43*, 1725–1749. [[CrossRef](#)]

44. Kang, W.; Minor, E.S.; Park, C.R.; Le, D. Effects of habitat structure, human disturbance, and habitat connectivity on urban forest bird communities. *Urban Ecosyst.* **2015**, *18*, 857–870. [[CrossRef](#)]
45. Hu, C.; Wu, W.; Zhou, X.; Wang, Z. Spatiotemporal changes in landscape patterns in karst mountainous regions based on the optimal landscape scale: A case study of Guiyang City in Guizhou Province, China. *Ecol. Indic.* **2023**, *150*, 110211. [[CrossRef](#)]
46. Paliwal, A.; Mathur, V.B. Spatial pattern analysis for quantification of landscape structure of Tadoba-Andhari Tiger Reserve, Central India. *J. For. Res.* **2014**, *25*, 185–192. [[CrossRef](#)]
47. Plexida, S.G.; Sfougaris, A.I.; Ispikoudis, I.P.; Papanastasis, V.P. Selecting landscape metrics as indicators of spatial heterogeneity—A comparison among Greek landscapes. *Int. J. Appl. Earth Obs. Geoinf.* **2014**, *26*, 26–35. [[CrossRef](#)]
48. Zhu, W.; Chen, J. The spatial analysis of digital economy and urban development: A case study in Hangzhou, China. *Cities* **2022**, *123*, 103563. [[CrossRef](#)]
49. Chen, G.; Widener, M.J.; Zhu, M.; Wang, C.C. Identification of priority areas for public-access automated external defibrillators (AEDs) in metropolitan areas: A case study in Hangzhou, China. *Appl. Geogr.* **2023**, *154*, 102922. [[CrossRef](#)]
50. Yue, W.; Qiu, S.; Xu, H.; Xu, L.; Zhang, L. Polycentric urban development and urban thermal environment: A case of Hangzhou, China. *Landsc. Urban Plan.* **2019**, *189*, 58–70. [[CrossRef](#)]
51. Liu, Y.; Yue, W.; Fan, P.; Peng, Y.; Zhang, Z. Financing China’s Suburbanization: Capital Accumulation through Suburban Land Development in Hangzhou. *Int. J. Urban Reg. Res.* **2017**, *40*, 1112–1133. [[CrossRef](#)]
52. Chao, F.; You, C.; Jin, W. Optimizing Urban Stock Space through District Boundary Reorganization: Hangzhou’s Administrative Adjustment. *Land* **2023**, *12*, 959. [[CrossRef](#)]
53. Qian, Z. Hangzhou. *Cities* **2015**, *48*, 42–54. [[CrossRef](#)]
54. Wang, G.; Yue, D.; Yu, Q.; Yang, D.; Xu, C.; Wang, F. Study on Forest and Grassland Ecological Space Structure in Eyu Mining Area and Potential Alternatives for Enhancing Carbon Sequestration. *Forests* **2023**, *14*, 1587. [[CrossRef](#)]

**Disclaimer/Publisher’s Note:** The statements, opinions and data contained in all publications are solely those of the individual author(s) and contributor(s) and not of MDPI and/or the editor(s). MDPI and/or the editor(s) disclaim responsibility for any injury to people or property resulting from any ideas, methods, instructions or products referred to in the content.